The impact of oxidation during curing of binder jetted 17-4 PH stainless steel on powder properties and powder surface chemistry

Citation for the original published paper (version of record):
Kazi, S., Zissel, K., Hryha, E. (2027). The impact of oxidation during curing of binder jetted 17-4 PH stainless steel on powder
properties and powder surface chemistry. Applied Surface Science, 752.
http://dx.doi.org/10.1016/j.apsusc.2026.168270

Applied Surface Science 752 (2027) 168270

Contents lists available at ScienceDirect

Applied Surface Science

journal homepage: www.elsevier.com/locate/apsusc

Full Length Article

The impact of oxidation during curing of binder jetted 17-4 PH stainless steel on powder properties and powder surface chemistry

Sofia Kazi [a,*], Kai Zissel [a,b], Eduard Hryha [a]

[a] Chalmers University of Technology, Department of Mechanical Engineering, Gothenburg, Sweden
[b] Linde GmbH, Unterschleißheim, Germany

ARTICLE INFO

Keywords:
Binder jettting
Powder reuse
Powder oxidation
Additive manufacturing
Surface chemistry
Curing
17-4 PH

ABSTRACT

Binder jetting is an additive manufacturing process that selectively joins powder particles with a liquid binder to create complex 3D objects. Achieving final material properties requires subsequent curing, debinding, and sintering. This study investigates the degradation mechanisms of 17-4 PH stainless steel powder during multiple reuse and curing cycles in the BJT process. X-ray photoelectron spectroscopy (XPS) is employed to analyze changes in the surface chemistry of the powders. XPS results demonstrate the increase of the oxide layer thickness from ~ 4.3 nm to ~ 7.1 nm with powder conditioning. After the first curing process, the oxide layer thickness increased to ~ 9.5 nm, but following curing cycles showcased minimal changes. These findings agree with bulk oxygen measurements, where the oxygen content increased from ~ 730 ppm of the unconditioned sample to ~ 1300 ppm after conditioning. After the first curing, the oxygen content rose to ~ 1500 ppm, whereas the subsequent curing did not alter the oxygen content much. The uptake of oxygen results in elevated flowability and packing behaviour due to the passivating oxide layer on the surface of the particles. The findings provide insights into the factors affecting powder reusability and the potential impact on the final part quality in BJT.

1. Introduction

Unlike traditional subtractive manufacturing methods that employ the removal of material to create a component, additive manufacturing (AM), often referred to as 3D printing, utilizes a layer-by-layer addition of material strategy to create a part. Complex geometries, often achieved through sophisticated CAD design, streamline production by eliminating the multi-step processes inherent in traditional manufacturing.

Binder Jetting (BJT) is an additive manufacturing (AM) process characterized by the selective deposition of a liquid bonding agent to join powdered materials. In this process, a layer of powder is evenly spread within a build chamber. Subsequently, a binder is precisely dispensed onto the powder bed, selectively adhering particles together according to the 3D model. This process is iteratively repeated, layer by layer, to construct the desired object within the powder bed. Subsequent steps, including curing, debinding and sintering, consolidate the part and achieve its final shape and desired material properties. Printed parts exhibit low initial density (approximately 50–60%), resulting in substantial linear shrinkage (around 10–20%) during the densification phase of sintering, where metal particles form metallic bonds via diffusion processes [1]. Furthermore, sintering is often conducted close to the melting point of the metal powder, potentially causing distortions in the part's external geometry. It has been shown that the shrinkages occurring during the sintering step are often anisotropic, with higher shrinkage in the building direction (z-axis) [2]. A lower layer thickness during printing can lead to higher green density and careful control of the liquid binder levels are needed to ensure proper adhesion on the particles [3]. In general, a high green density is wanted as a higher powder packing requires less densification, leading to less shrinkage and often higher sintered densities [4].

Particle size distribution (PSD) exerts great influence across the entire binder jetting process. PSD significantly impacts the packing, sinterability and surface finish of both the green (unsintered) and the final part. Finer powders generally yield smoother surfaces. On the other hand, fine powders are characterized by a large surface area and hence higher chemical reactivity and inter-particle interaction, such as capillary and Van der Waals forces and cohesion, leading to a decrease in powder flowability and poorer packing characteristics [5]. As fine and spherical gas-atomized powders for BJT tend to have a high cohesion and poor flowability [1,6,7], they often require powder conditioning to

* Corresponding author.
E-mail address: sofiakaz@chalmers.se (S. Kazi).

https://doi.org/10.1016/j.apsusc.2026.168270
Received 5 March 2026; Received in revised form 24 July 2026; Accepted 29 August 2026
Available online 30 August 2026

Table 1
Chemical composition of powder in wt.% specified by supplier [23].

Powder	Fe	Cr	Ni	Cu	C	Mn	Nb + Ta	Si	S
17-4 PH	Balance	15.5–17.5	3.0–5.0	3.0–5.0	0.07 (max)	1.0 (max)	0.15–0.45	1.0 (max)	0.03 (max)

reach adequate flow properties for printing after the atomization process. The conditioning typically involves a heat treatment to dry or oxidize the powder or a combination of both. Barthel et al. [8] reported that powder drying reduces powder cohesion and enhances powder flowability. Janzen et al. [9] demonstrated that drying of Ti-6Al-4 V notably improved the powder flowability and quality of the green parts. The authors recommended drying new powder due to undefined delivery and storage times [9].

Optimal packing, frequently achieved with bimodal distributions (combining large and small particles), is crucial for maximizing binder saturation [7]. This ensures that the binder effectively infiltrates the powder bed. Furthermore, the PSD dictates the appropriate layer thickness during printing. Finer powders often necessitate thinner layers to ensure proper binder penetration and prevent voids. Lower PSD also leads to better sinterability. Finer particles exhibit accelerated sintering kinetics due to their high surface area, resulting in faster densification and potentially shorter sintering times [10]. However, while faster sintering is advantageous, it can also lead to greater part shrinkage. The initial green density, which is heavily influenced by the PSD and packing, plays a crucial role in controlling this shrinkage.

Although tailoring the powder characteristics, such as flowability, to achieve high powder packing during printing was the focus of previous research, an equally important aspect remains the reusability of unbound BJT powders, which are collected after depowdering and reused for following printing cycles. Coarsening of 316 L stainless steel powder has been observed due to the powder being reused 16 times, thus resulting in higher flowability [11]. Similarly, a loss of fine particles was found for 17-4 PH stainless steel after powder reuse [12].

The effect of powder reuse in AM technologies on powder properties have reported an increase in surface oxidation and higher bulk oxygen levels, mainly attributed to the elevated temperatures in the build chamber and interactions with the energy source during particle melting and fusion [13–15]. On the other hand, BJT is considered a “cold process”, with printing being conducted at room temperatures and the studies on powder reuse in this technology have mostly reported changes in the PSD and powder flowability over multiple reuse cycles but have not investigated the direct influence of the curing process on powder characteristics in detail. The curing process is, however, a form of powder conditioning, as the loose powder is subjected to heat treatment. Curing is often conducted in ambient conditions, where oxygen present in the air can lead to oxidation of the powder. It was shown that curing of tool steel in air led to powder oxidation, which in turn increased the difficulty of depowdering and lowered sintered densities [16].

An equally important aspect remains the reusability of powder during sequential printing cycles. Coarsening of the powder was observed, thus resulting in better flowability [11]. It has long been argued that changes in the surface chemistry of powders for additive manufacturing, accompanied by oxide layer growth and enrichment in oxide particulates on powder surfaces, can impact the printed part quality as well as the reusability of the powder. Previous studies have analyzed the effect of the atomization process on the particle shape, surface chemistry and flowability of 316 L powders [17,18]. In steels, the presence of Cr and Mn leads to the formation of stable oxides due to the elements’ high affinity to oxygen [19]. The monitoring of the processing atmosphere during sintering cycles, as well as adjusting the sintering conditions, enables the reduction of stable oxides on the surface of PM-steel powder particles [20].

Recent advancements in the BJT of 17-4 PH stainless steel have highlighted the critical role that powder oxidation plays throughout the manufacturing lifecycle. Notably, a previous two-part study [21,22] demonstrated that the oxygen concentration in the atmosphere during debinding influences binder removal and powder oxidation. It was shown that powder oxidation during debinding at 300 °C for 2 h is detrimental to the final sintered oxygen content of the stainless steel. While these studies demonstrated that powder oxidation during debinding affects the bulk oxygen content, the influence of powder degradation during curing on powder properties relevant to the printing process remains insufficiently understood. Understanding the exact powder degradation mechanism requires highly sensitive surface characterization.

To bridge this gap, this study introduces X-ray photoelectron spectroscopy (XPS) to investigate the impact of conditioning, ambient air curing, and powder reuse on the powder surface chemistry and rheological properties of 17-4 PH stainless steel. The rheological properties of the powder were compared for unconditioned, virgin, and reused powder subjected to four curing cycles at 200 °C for 4 h. The changes in the powder surface chemistry, morphology, and bulk chemistry were investigated after each curing cycle.

2. Materials and methods

2.1. Materials and printing

N_2-atomized pre-alloyed 17-4 PH stainless steel powder (Desktop Metal Inc., USA) was studied in this work. The powder elemental composition specified by the supplier is depicted in Table 1. The powder had a PSD of D_{10} = 6.5 µm, D_{50} = 14.3 µm and D_{90} = 26 µm measured using a Camsizer X2 employed with dynamic image analysis (ISO 13322–2, Microtrac).

Fine gas-atomized powders tend to be too cohesive and cannot be used directly for BJT printing. To ensure adequate powder cohesion and flowability for printing, “unconditioned” powders are oxidized to increase the flowability. The conditioned powder is considered virgin powder before printing, which is the standard condition received from the supplier. Unconditioned powder was also studied to understand the impact of powder conditioning on surface chemistry and powder rheology.

A Production System™ P-1 (Desktop Metal Inc., USA) was employed for BJT printing. A water-based binder (SPJ-04, Desktop Metal Inc., USA) was applied for printing. Besides water, the binder contained solvents and a thermoset polymer. The printer includes O_2 and humidity control sensors and gas purging of the build chamber. The build job layout in this study consisted of 15 cuboid green samples with nominal dimensions of 10 x 10 x 10 mm^3. The green samples were used to examine the influence of curing on the printed green density. A precision scale (QUINTIX224-S1, Sartorius AG, Germany) with a resolution of 0.001 g was used to obtain the mass of each green sample. The volume of each green sample was calculated based on the measurements of the dimensions in X-, Y- and Z-direction via a micrometer screw gauge with a resolution of 0.001 mm. Virgin powder was loaded into the printer and reused for 5 build jobs, followed by curing the 5 obtained build boxes simultaneously.

The build boxes were cured in a forced air-convection furnace (TR 120 LS, Nabertherm GmbH, Germany). A heating rate of 1.5 °C/min to a maximum temperature of 200 °C was applied and a dwell time of 4 h was set. Natural cooling of the furnace was taking place after the dwell time. After curing, the green samples were separated from the loose powder bed inside an inert environment with tools such as brushes and tweezers. After rough depowdering with tools, compressed air or gas was used to

Table 2
The annotation of the samples based on the amount of print jobs and curing cycles.

Sample name	Total no. of print jobs	No. of curing processes
Unconditioned	–	–
Virgin	–	–
C1	5	1
C2	10	2
C3	15	3
C4	20	4

Table 3
XPS binding energies in eV, measured on pure metallic and oxides standards on as-received surface and after etching.

Peak	Peak position on the as-received surface	FWHM on the as-received surface	Peak position after etching at 100 nm	FWHM after etching at 100 nm
$Fe2p_{3/2}$ (plate)	710.8	3.8	706.8	1.03
$Fe2p_{3/2}$ (Fe_2O_3)	710.8	3.55	708.8	3.8
O1s (Fe_2O_3)	529.9	1.25	529.8	1.03
$Cr2p_{3/2}$ (plate)	576.7	3.2	574.3	0.92
$Cr2p_{3/2}$ (Cr_2O_3)	576.7	3.2	575.7	4.1
O1s (Cr_2O_3)	530.5	1.19	530.8	1.73
$Mn2p_{3/2}$ (plate)	641.5	3.5	638.8	0.94
Si2p (Si-wafer)	102.6	1.8	98.9	1.1
O1s (Si-wafer)	532	1.8	532	1.6
$Nb3d_{5/2}$ (Nb-powder)	207.2	1.18	202.3	1.05
O1s (Nb-powder)	530.8	1.7	530.7	1.6

get rid of the remaining powder. The powder collected from depowdering was reloaded after sieving with a 43 μm mesh into the printer and reused for 5 consecutive build jobs. This was repeated until 20 build jobs were completed, which led to four curing cycles in total. No additional virgin powder has been added during the subsequent printing cycles. Powder samples were taken after each curing and sieving cycle.

Consequently, the powders used for investigation in this work consisted of unconditioned powder (before any oxidation), virgin powder (after conditioning and before printing) that was loaded into the machine before the first print job and sieved powders collected from depowdering after each curing cycle (C1-4). Table 2 summarizes the collected samples used in this work, where C1-4 described the amount of curing cycles the powder was subjected to.

2.2. Powder characterization

High-resolution scanning electron microscopy (HR-SEM) was employed to study the surface morphology of the particles (Leo Gemini 450 SEM, Zeiss GmbH, Germany), equipped with a field emission gun and In-lens detector. An accelerating voltage of 15 kV and working distance of 4.0 mm were used to investigate the surface of the particles. Due to the particle size, carbon tape (3 mm) was deemed the safest option to press the powder onto the sample holder to avoid particles escaping in the vacuum chamber. The bulk oxygen and nitrogen contents of each powder sample were measured by an ONH analyzer (ONH836, LECO Corporation, USA) based on the carrier gas hot extraction method. The humidity of the powder samples was determined via Karl Fischer titration (C30S Compact KF Coulometer, Mettler-Toledo GmbH, Germany).

Table 4
Particle size distribution for different powder conditions.

Sample	D_{10} (μm)	D_{50} (μm)	D_{90} (μm)
Virgin	6.3	14.7	27.6
C1	6.3	15.1	28.4
C2	6.4	15.1	28.1
C3	6.5	15.7	28.3
C4	6.5	15.5	30

The rheological behavior of the unconditioned, virgin and C4 powders was studied using a Revolution Powder Analyzer (Mercury Scientific Inc., USA). The Revolution Powder Analyzer (RPA) entails a setup with a transparent drum filled with material, which rotates according to parameters set by the user. On the other side of the setup, a camera captures the rotation of the material, which is illuminated by a light source. The surface area of the material is captured by the camera and analyzed in specialized image analysis software. Equal powder volumes of 100 ml were freely loaded in the drum. The rheological tests were performed in ambient conditions. Multi-flow experiments were performed, varying the drum rotation speed from 1 to 69 RPM with 2 RPM increments. At each rotation speed, 150 powder avalanches were analyzed. Each powder sample was measured in triplicate to ensure reliability. Packing characteristics were also determined for each powder sample, where tap and apparent densities were measured by vibrating the drum for ten cycles.

To investigate the changes in the surface chemistry of the powder in terms of oxide layer thickness and composition, X-ray photoelectron Spectroscopy (XPS) was carried out utilizing PHI 5000 (Physical Electronics, MN, USA) equipped with a monochromator Al Kα source (1486.6 eV) with lateral resolution of analysis of 100 μm. Survey scans, as well as narrow elemental scans, were performed using 224 eV and 26 eV pass energy, respectively. Energy calibration had previously taken place with reference to $Au4f_{7/2}$ (83.95 eV), $Ag\ 3d_{5/2}$ (368.21 eV) and $Cu\ 2p_{3/2}$ (932.62 eV) peaks. High purity oxide powder and standard plates were also measured and their peak characteristics can be seen in Table 3. High-resolution XPS spectra (Fe2p, Cr2p, Mn2p, Nb3d, Si2p and O1s) were deconvoluted using a Shirley background. Peak fitting was performed using Assymetric profiles. Additionally, while monatomic Ar^+ bombardment is an established depth-profiling technique, it is known to induce preferential sputtering artifacts, occasionally reducing transition metal oxides (such as Fe_2O_3) to lower valence states. Consequently, while absolute thickness values may be subject to minor underestimations, the relative oxidation trends between curing cycles remain strictly reliable. For depth profiling, etching of the powder surface was performed on a 2 mm x 2 mm area and down to 100 nm in depth using an Ar + ion gun, where the etch rate was calibrated using a Ta_2O_5 foil with known oxide layer thickness. Therefore, the etch depth and oxide thickness in this work are presented in Ta_2O_5 units. The data obtained was analyzed using the PHI MultiPak software.

To quantify the oxide layer thickness of the BJT powders, depth profiling data was evaluated using an established geometric correction model for spherical particles. Standard planar attenuation models are insufficient for powders due to variations in the electron take-off angle and non-uniform ion etching across curved surfaces. To account for this, the mathematical model derived by [24,25] integrates the angular dependence of the X-ray flux, photoelectron intensity, and localized etch rate over a spherical geometry. Based on this spherical integration, the interface broadening caused by curvature is corrected by defining the true radial oxide thickness as the specific sputter depth at which the normalized metallic intensity reaches 65% of its maximum value.

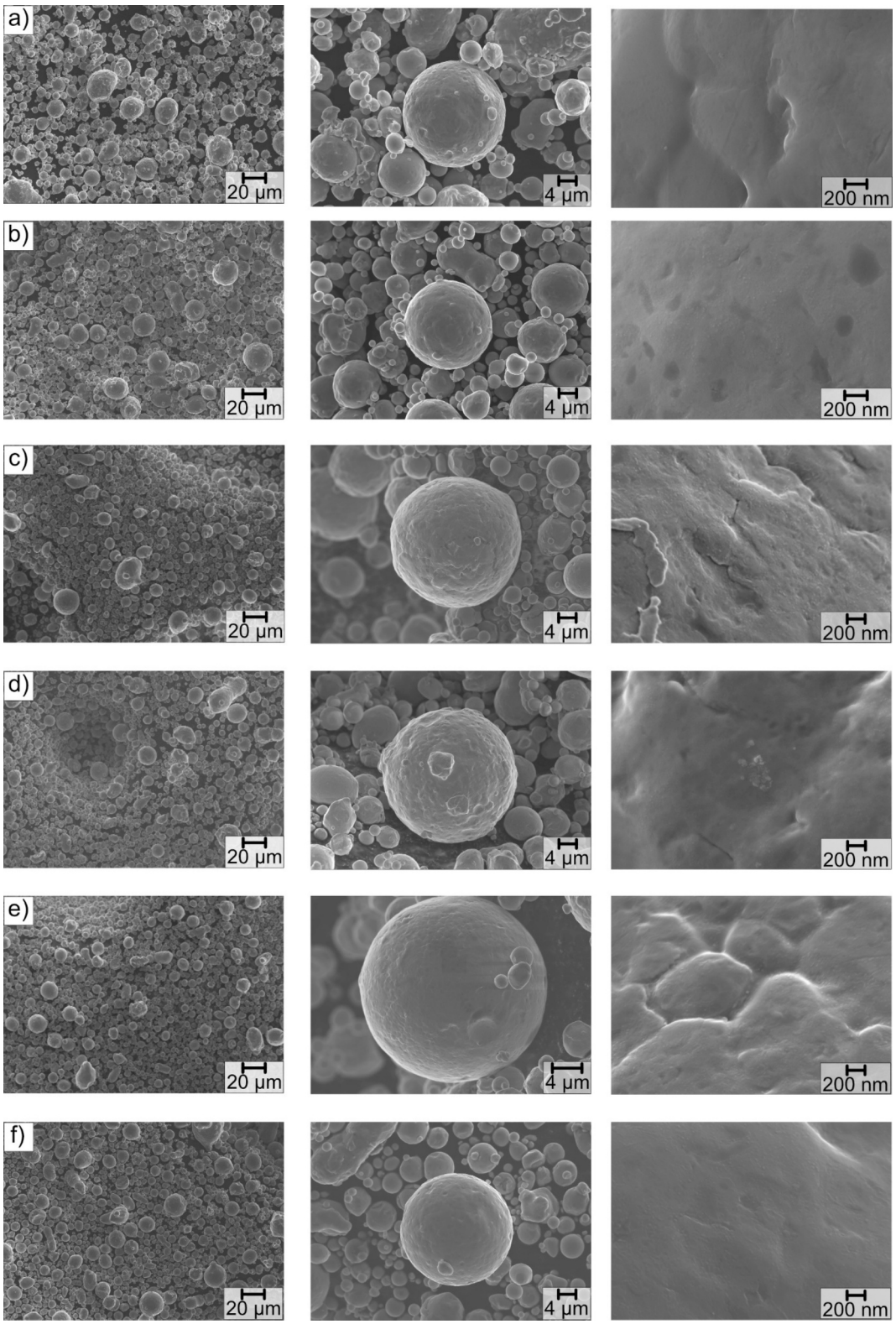

Fig. 1. SEM micrographs of the powder samples with each row corresponding to a) unconditioned, b) virgin, c) C1, d) C2, e) C3, f) C4 powders.

3. Results

3.1. Powder morphology

The particle size distribution of the different 17-4 PH powder samples is listed in Table 4. The D10 shows a minor increase by ~ 0.2 µm from virgin powder to powder sample C4 after 20 build jobs. The D50 exhibited a minor increase from 14.7 µm to 15.5 µm from virgin powder to powder sample C4. The largest increase was measured for the D90 from 27.6 µm for the virgin powder to 30 µm for powder sample C4.

SEM imaging was employed to observe the surface of the powder samples. At low magnification, all samples seem to comprise mostly

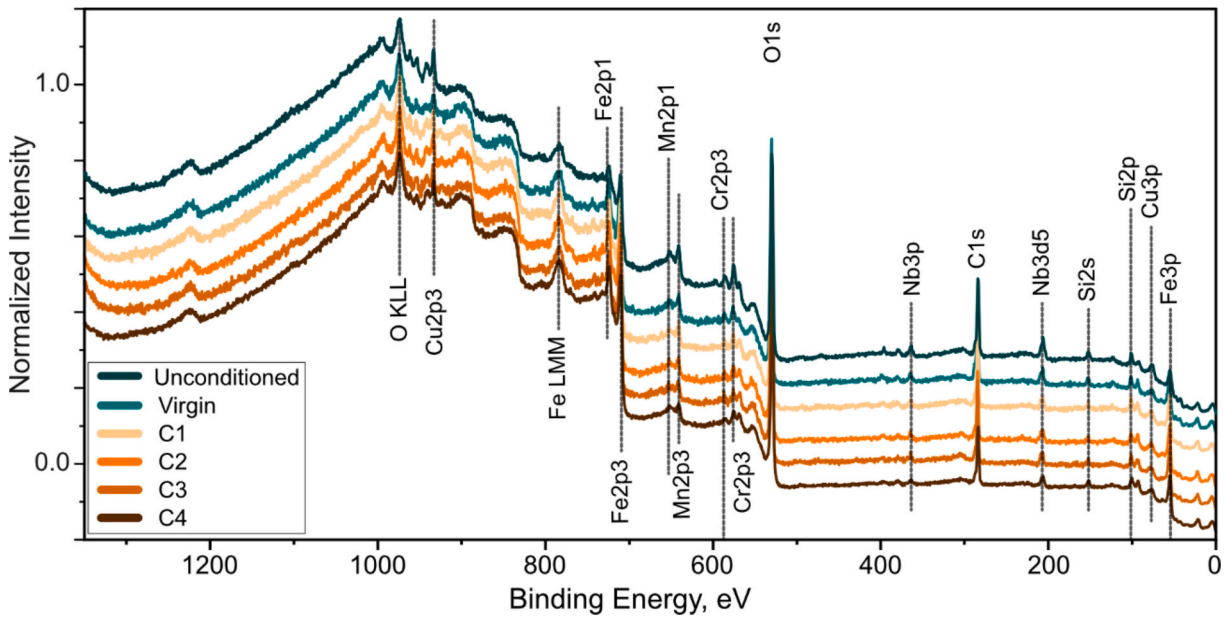

Fig. 2. XPS survey spectra of powder samples used in this study showcasing the strong presence of Fe2p, Cr2p, Mn2p, Nb3d, Si2p, O1s on the as-received surface.

spherical powders with the presence of satellites. It seems that the presence of satellites and agglomerates is more severe in the unconditioned sample (Fig. 1 (a) first and second column). The powder surface does not present noticeable differences from unconditioned to virgin state, and later with curing (Fig. 1 (a), (b), (f) second and third column).

3.2. Bulk and surface chemistry of the powder

X-ray photoelectron spectroscopy (XPS) is a highly surface-sensitive technique used to analyze the chemical composition and estimate the oxide layer thickness of powder particles. Fig. 2 shows survey spectra for all samples, clearly revealing the presence of iron (Fe2p), chromium (Cr2p), manganese (Mn2p), silicon (Si2p), niobium (Nb3d5), and carbon (C1s). Despite a high nickel (Ni) content in the bulk powder (Table 1), the corresponding Ni peaks are absent in the surface spectra. This suggests that nickel is either absent or present in very low concentrations in the outermost oxide layer. Conversely, Mn is significantly enriched on the powder surface. This surface enrichment of manganese is a common phenomenon, even when present in trace amounts in the bulk, due to its strong affinity for oxygen [26]. The carbon (C1s) peak is attributed to adsorbed carbon species, a typical surface contaminant resulting from exposure to air.

Due to the presence of many elements on the surface of the powders, the identification of chemical states is difficult. Pure metal standards of Fe, Cr and Mn (purity > 99.9%), as well as standard oxides of Fe_2O_3 and Cr_2O_3 (>99% Sigma Aldrich), were analyzed in order to identify the peak characteristics for metals and their cations (Table 3). The silicon peak characteristics were identified using a silicon wafer. All XPS depth profiling spectra (Fig. 3) were corrected by using the peak position of adventitious carbon at 284.8 eV at the as-received surface.

XPS narrow scans of each of the elements present on the surface of the powders were recorded as seen in Fig. 3. Steel powders tend to form a homogeneous iron base oxide layer with the presence of particulate oxide features, size and composition of which are determined by the powder composition, powder atomization and handling. The iron Fe2p3/2 peak position located at ~ 710.8 eV suggests the predominant presence of Fe_2O_3 on the surface. In the unconditioned sample (Fig. 3 (a)), a small peak located at 706.8 eV indicative of the Fe^{met} peak can be observed at the as-received surface, suggesting the presence of a thin oxide layer below $3\lambda_{ox}$ (λ_{ox} = 1.5 nm being the attenuation length or mean free path of the valence electron in Fe_2O_3). This peak is absent in the virgin and C1-4 samples, indicating the presence of a thicker oxide layer (XPS narrow scans of samples C1, C2, C3 can be found in Supplementary Information). The surface oxide is also enriched with chromium and manganese in the oxidized state. Silicon, which is very low in the composition (Table 1), is present in an oxidized state as well but is etched out after 5 nm. In addition, O1s spectra showcase a stronger contribution at ~ 532 eV on the top surface, which is characteristic of the presence of silicon-based oxide, and this shoulder is decreasing proportionally to the Si-peak decrease.

Focusing on the Fe2p spectra in the unconditioned sample (Fig. 3 (a)), the Fe^{met} peak at 706.8 eV is starting to become noticeable and a lot higher in intensity than the Fe^{2+} and Fe^{3+} peaks at 5 nm, thus indicating the oxide layer is lower than 5 nm. For the virgin sample (Fig. 3(b)), the Fe^{met} peak is noticeable at 5 nm and by 10 nm also higher in intensity than the Fe^{2+} and Fe^{3+} peaks. Though the same trend can be observed in the C4 sample (Fig. 3(c)) with the Fe^{met} having high intensity at 10 nm, the intensity of the peak at 5 nm is barely noticeable. Hence, it can be concluded that the iron-base oxide layer is lower than 10 nm in both the virgin and C4 samples, with higher thickness in the C4 sample. The Cr2p spectra present a different trend for the three samples depicted. In the unconditioned sample (Fig. 3(a) second row), the Cr^{met} peak (574.3 eV) reaches higher intensity than the Cr^{3+} peak at 5 nm, whereas in the virgin sample (Fig. 3(b) second row) it is at 10 nm. In the C4 sample (Fig. 3(c)), the oxidized state of Cr is etched out after 10 nm, indicating that Cr is present in the oxidized state either as part of an iron-rich homogeneous oxide layer [27] or in the form of fine oxide particulates, or both. For Mn2p spectra, Mn is present in the oxidized state and even after 100 nm of etching, it never reaches its metallic state but is rather etched away, confirming its segregation on the powder surface [26]. Traces of Nb are found in the first 10 nm of etching, located at ~ 207.1 eV for the $Nb3d_{5/2}$ peak and at ~ 209.8 eV $Nb3d_{3/2}$ (with a characteristic $\Delta E = 2.7$ eV due to the split spin–orbit nature of the Nb3d region), presumed to be Nb_2O_5 according to the literature [28,29].

Fig. 4(a) exhibits the development of oxygen O1s peak intensity with etch depth for each powder studied. From the etch profiles, it is evident that most of the oxygen is removed in the first 20 nm of etching and in the virgin sample, 50% of oxygen is removed before 10 nm. Analysis of the normalized oxygen profile indicates an increase in the iron-based oxide layer thickness from virgin powder with increasing powder reuse, showing the lowest thickness of the iron oxide and continuously increasing from C1 to C4.

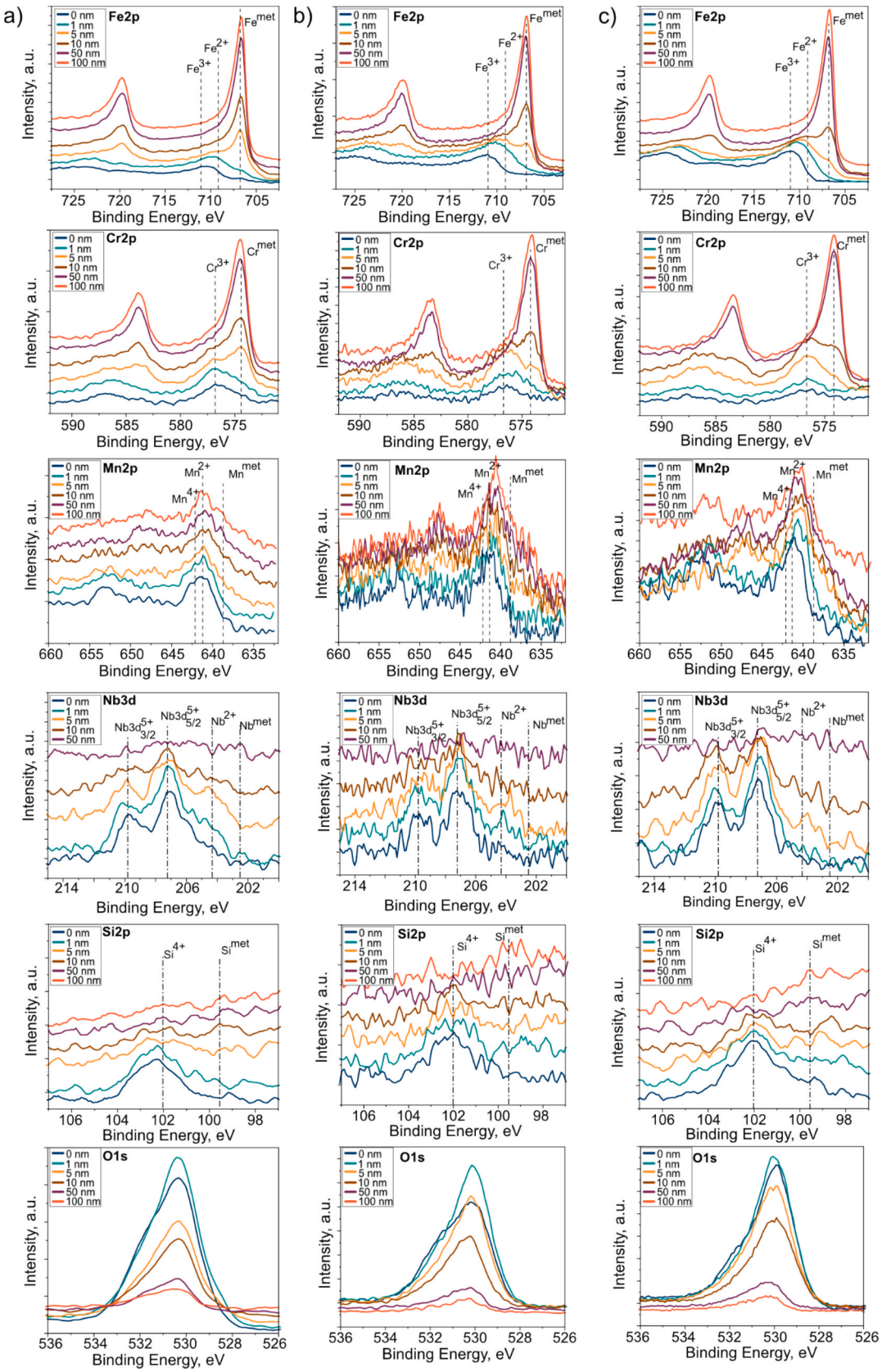

Fig. 3. High-resolution XPS narrow scans of Fe2p, Cr2p, Mn2p, Nb3d, Si2p, O1s (top to bottom) for the a) unconditioned, b) virgin, c) C4 powder samples (left to right).

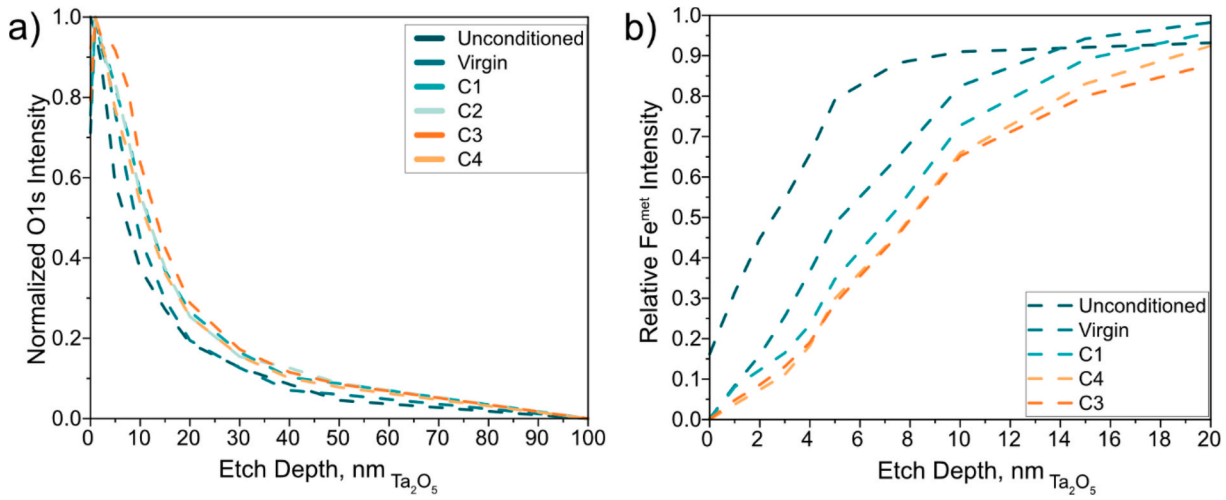

Fig. 4. a) Normalized oxygen intensity with etch depth, b) Normalized Fe^{met} intensity across etch depths. The etch rates and, therefore, etch depths were calibrated using a Ta_2O_5 foil.

Table 5
Approximate Oxide layer thickness measured for each sample.

Sample	Oxide layer thickness (nm), according to Fe^{met} peak	Oxide layer thickness (nm), according to O1s peak
Unconditioned	4.3 ± 0.20	6.0 ± 0.50
Virgin	7.1 ± 0.15	8.7 ± 0.3
C1	9.5 ± 0.30	11.2 ± 0.2
C2	9.7 ± 0.15	11.6 ± 0.3
C3	10.0 ± 0.23	12.0 ± 0.2
C4	9.8 ± 0.25	11.5 ± 0.1

Table 6
Total humidity content of the different powder samples.

Sample	Humidity (ppm)
Virgin	44 ± 3
C1	43 ± 5
C2	62 ± 1
C3	56 ± 1
C4	54 ± 2

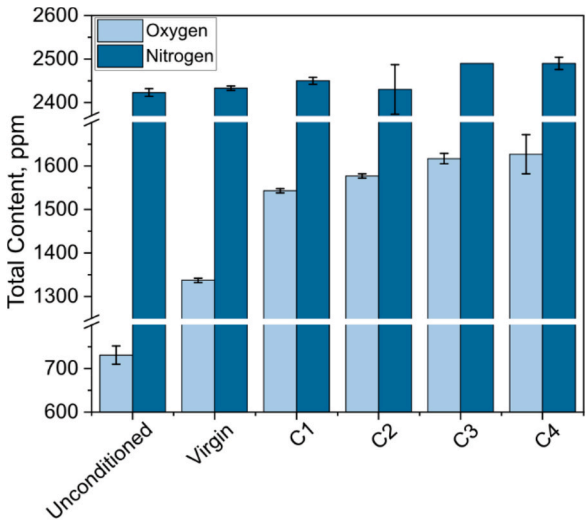

Fig. 5. Total oxygen and nitrogen content of the measured powders.

The oxide layer thickness was measured by using the relative intensity of metallic iron Fe^0 peaks at different etch depths normalized to the intensity at the etch depth where Fe cation peaks disappear, $I_0/I_{0\text{-}100}$ (where I_0 is the intensity of the metallic peak at each depth and $I_{0\text{-}100}$ is the intensity of the metallic peak at the depth where only the metallic state of the element is present, 100 nm in case of presented measurements). Due to the absence of any Fe^0 peak at the as-received surface across all samples after conditioning, the oxide layer thickness is estimated to be more than $3\lambda_{ox}$. The oxide layer thickness was calculated by taking the normalized intensity at the etch depth that had a value of 65% (Table 5). By following this model [24,25], it was estimated that the oxide layer thickness in the unconditioned powder was ~ 4.3 nm, whereas in the virgin powder it was approximately 7.1 nm. The oxide layer thickness showed a first sharp increase with curing from 7.1 to 9.5 nm, in line with the oxygen content, see Fig. 2, with a much slower increase with further reuse and curing, from 9.5 to 10 nm from C1 to C3 and C4, indicating powder passivation. The C1-C4 powders exhibit very small variations in oxide layer thickness calculations as indicated by the deviations in the table. A second method to calculate the oxide layer thickness was used, by using the relative intensity of O1s peak at 50% from its max intensity, with values also presented in Table 5. The difference in values calculated between the two methods is that first takes into account just the thickness of the Fe-rich oxide layer, while the latter accounts for the contribution of secondary phases such as the fine oxide particulates and does not account for surface roughness on top of the particles.

Bulk oxygen and nitrogen content measurements are exhibited in Fig. 5. The measurements revealed the lowest oxygen content in the unconditioned powder sample at ~ 730 ppm. A significant uptake is recorded after conditioning of the powder, and evidently, the virgin powder has an oxygen content at ~ 1300 ppm. After the first curing cycle, the oxygen increased to ~ 1500 ppm and remained in that range throughout the whole process. The nitrogen content experienced negligent variations before and after conditioning, remaining stable at ~ 2420–2490 ppm. The humidity of the different 17-4 PH powder samples is given in Table 6. The humidity content of the powder ranges from ~ 43 ppm to ~ 62 ppm. The virgin powder shows similar humidity content to the powder sample C1, while powder samples C2 to C4 exhibited slightly higher values. With the second curing cycle there is a noticeable increase in humidity that seems to be alleviated with further curing cycles, as can be seen in samples C3 and C4.

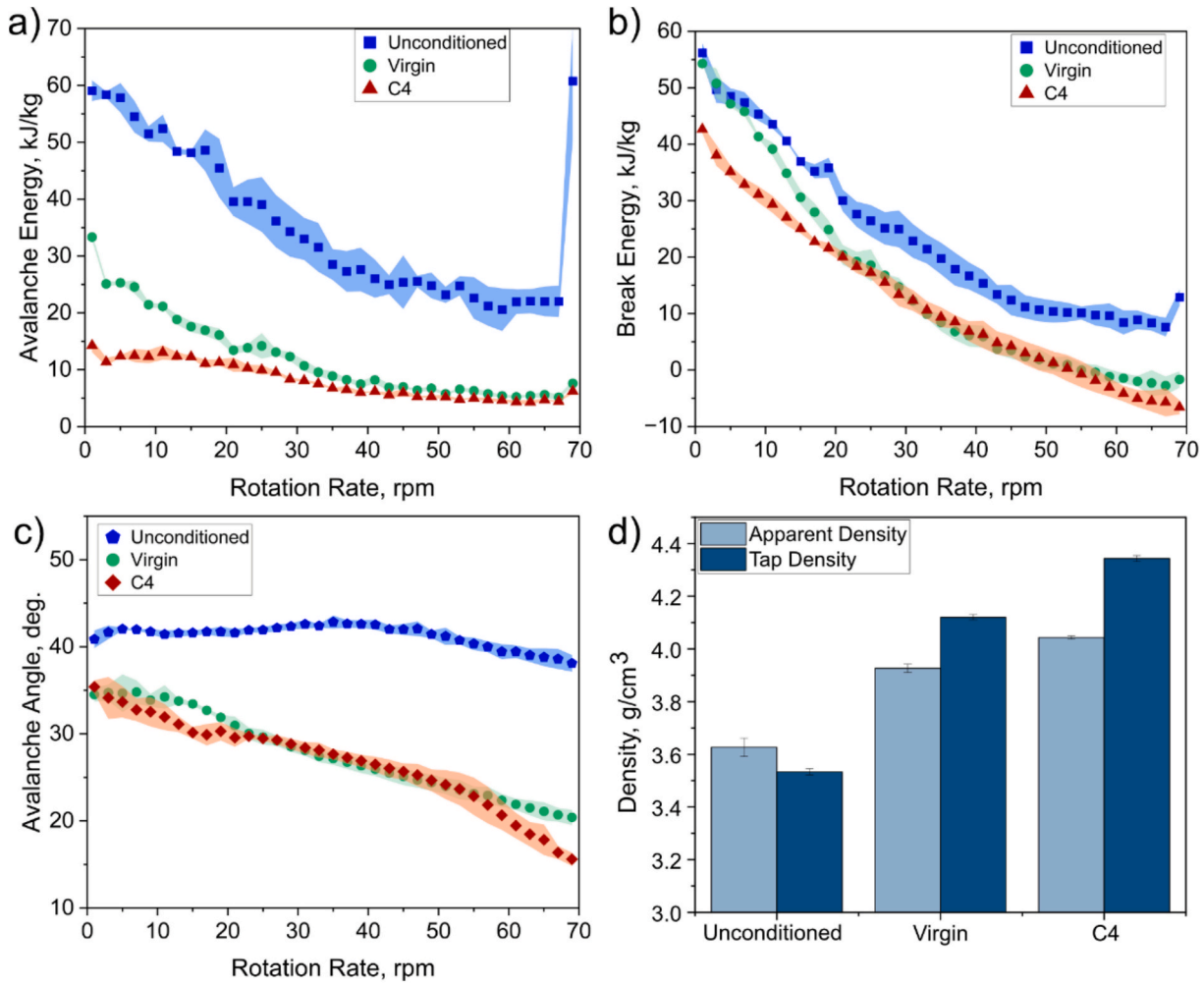

Fig. 6. Multi-flow test metrics, a) avalanche energy, b) break energy and c) avalanche angle, measured with a 2 rpm step in the 1–69 rpm range, error bars are shown as filled colors that represent the standard deviation (2σ) from the three measurements, d) average apparent and tap densities measured by the RPA packing test with standard deviations, error bars represent the 2σ error.

3.3. Powder rheology

The unconditioned, virgin and most reused C4 powders were used for flowability measurements. Generally, better flowing powders yield lower avalanche and break values. It can be observed in Fig. 6 that the unconditioned sample exhibits the worst flowability with the highest energy and angle values coupled with the lowest densities compared to the other powder samples. In the unconditioned state, the powder presents with the most elevated avalanche angle values that have little to no variation with increasing rotating speed, indicating a quite persistent internal friction between the particles across all rotating speeds. After conditioning, the virgin powder shows a steep decrease in avalanche energy, an indication that the powder surface has formed a passivating layer aiding it to flow better. Break energy is also lower overall. C4 presents with lower values for avalanche and break energy than both the virgin and the unconditioned powders, easily discernible at low rotating speeds that are more representative of a powder's rheological behavior during printing. In the first 20 rpm, the avalanche angle also presents slightly lower values for the C4 sample compared to the virgin. Both apparent and tap densities increase with conditioning and curing of the powder.

3.4. Green density

The measured green densities for the different powder conditions are depicted in Fig. 7. A clear decrease in the green densities is evident after the first curing process from 4.71 ± 0.03 g/cm^3 for the virgin powder to 4.60 ± 0.04 g/cm^3 for C1. Printing with C2 powder resulted in similar green densities as printing with C1 powder. Printing with C3 powder showed a further decrease to 4.49 ± 0.08 g/cm^3, where a higher standard deviation was present.

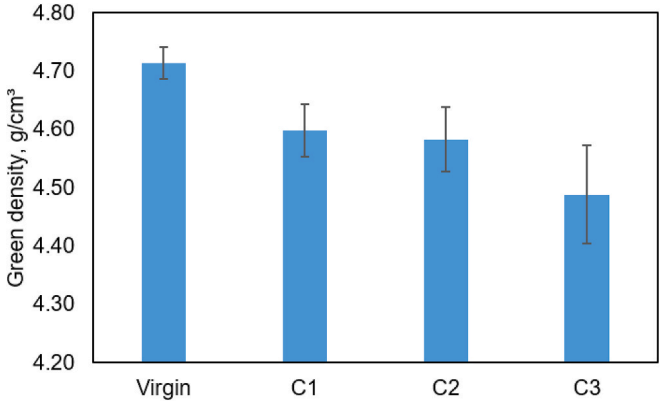

Fig. 7. Green densities based on the powder condition used for printing.

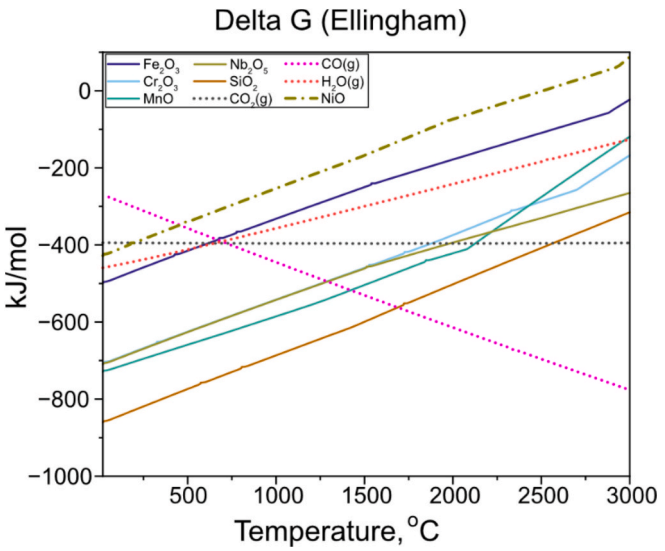

Fig. 8. Standard Gibbs free energies of formation (ΔG_f) for Fe_2O_3, Cr_2O_3, MnO, Nb_2O_5, SiO_2, NiO (plotted with HSC Chemistry software).

4. Discussion

4.1. Powder properties

This study sought to investigate the effect of curing on powder characteristics during consecutive binder jetting printing cycles. The dominant phenomenon taking place in the curing process is oxidation that alters the surface chemistry of the powder and positively impacts the rheological behavior. All the samples are covered by a Fe-based oxide layer, consisting primarily of Fe_2O_3 with the potential presence of some Cr_2O_3 [27], whose fraction is increasing with curing. A presence of fine oxide features sizing < 20 nm composed of strong oxide formers like Cr, Mn, and Si across the powder's surface was observed, as seen in previous studies [26,30]. The surface oxide layer also contains some Nb in the oxide state as it is a strong oxide former [31].

The standard Gibbs free energies of formation (ΔG_f) for Fe_2O_3, Cr_2O_3, MnO, Nb_2O_5, SiO_2 are significantly more negative than that of NiO. Hence, the selective oxidation of Cr, Mn, and Fe (as well as Si and Nb since they exist at lower concentrations in the composition) is thermodynamically favored (Fig. 8). Consequently, Ni is not oxidized and does not segregate to the surface, remaining depleted in the outermost passivating layer.

The as-atomized unconditioned powder exhibits the lowest oxide layer thickness and oxygen content, which would be a positive characteristic and would aid in the printing of high-quality parts. In this case,

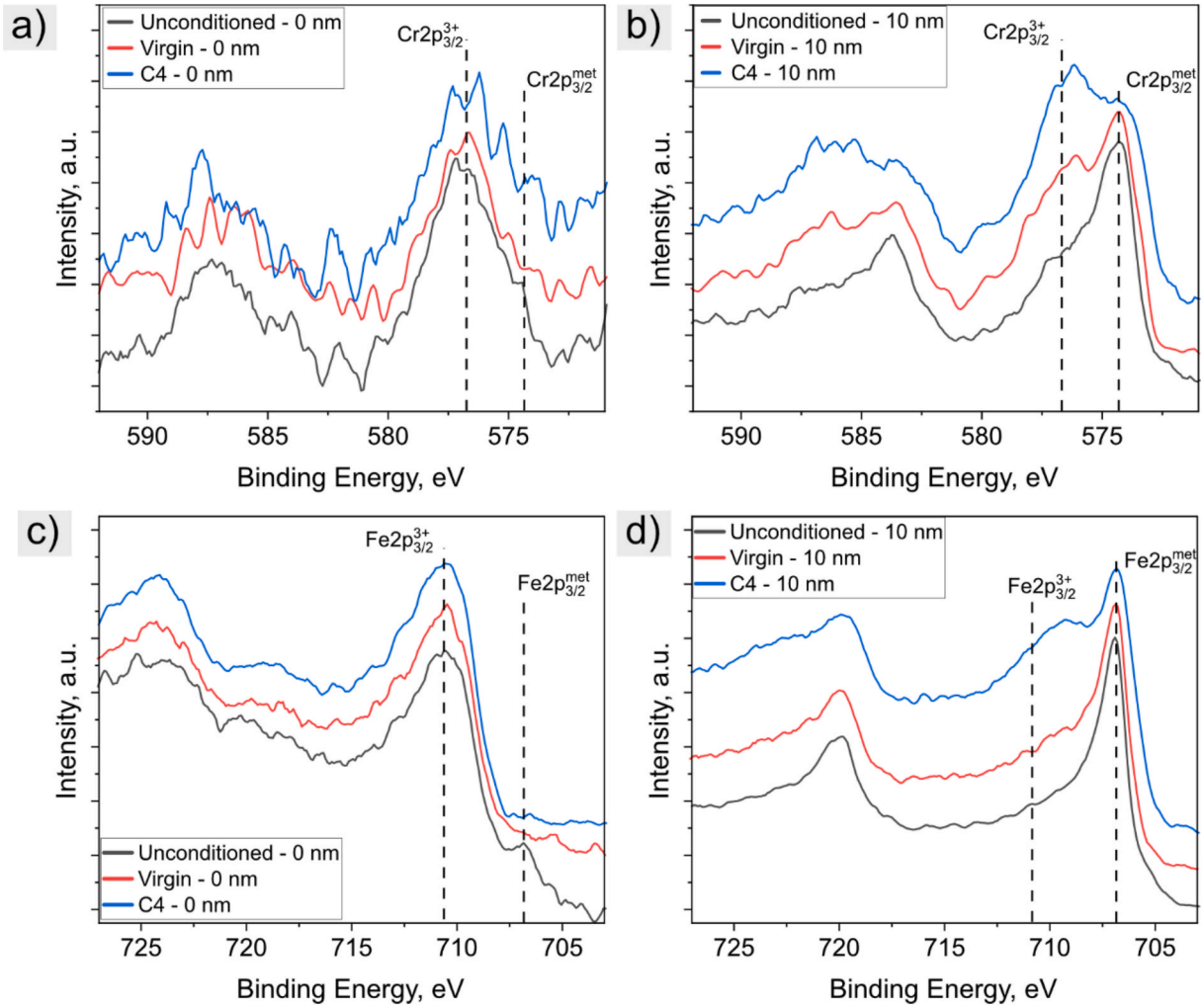

Fig. 9. Comparison of Cr2p spectra between the as-received (a) surfaces of the powders and after etching at 10 nm (b). Comparison of Fe2p spectra between the as-received (c) surfaces of the powders and after etching at 10 nm (d).

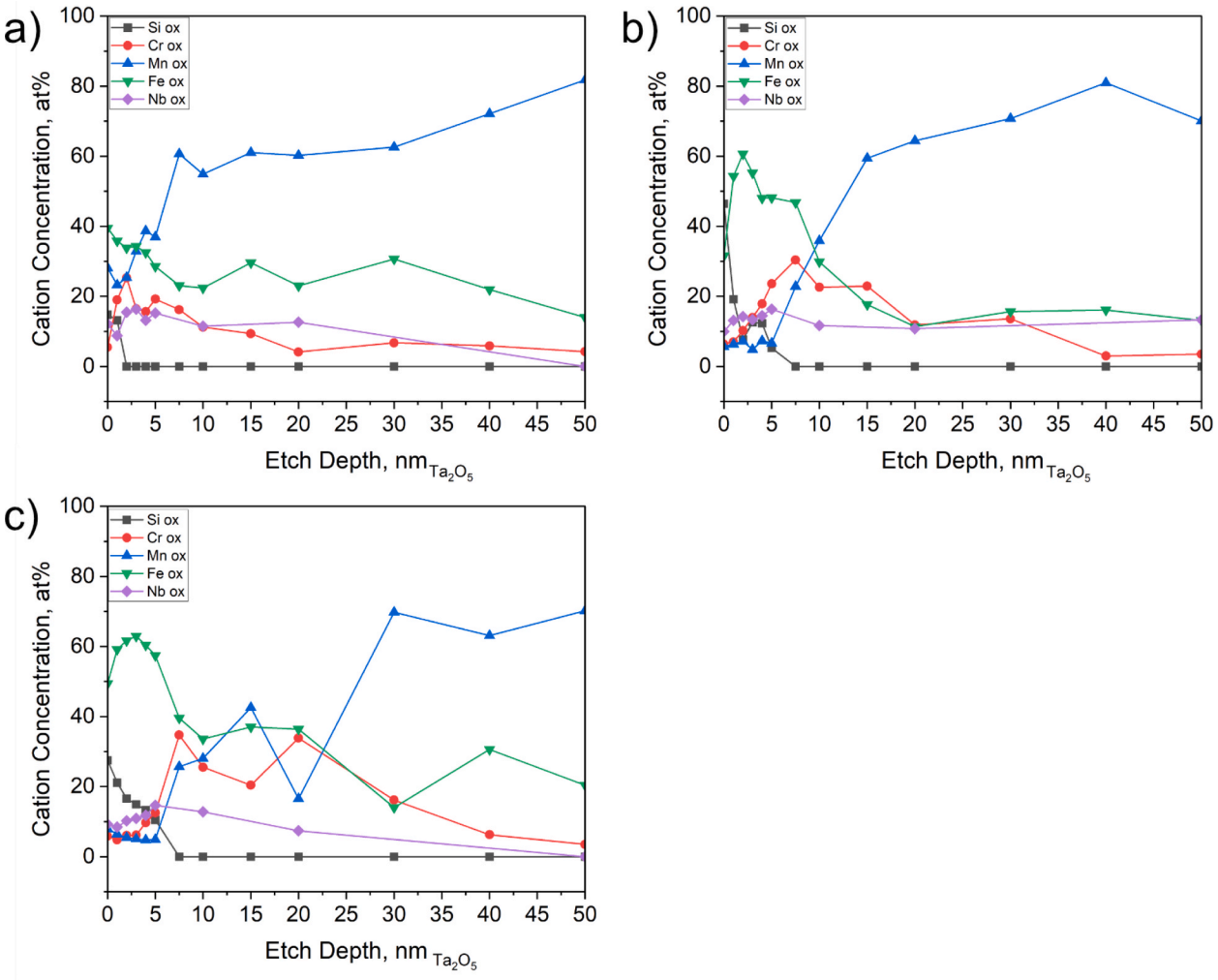

Fig. 10. XPS depth profile of cation concentrations of a) unconditioned, b) virgin, c) C4 powers.

due to the small PSD of the powder used in BJT, the unconditioned powder is too cohesive to flow, leading to low packing of the powder bed. Therefore, a conditioning step is added to the powder preparation before printing in order to decrease the cohesion of the powder. The virgin powder possesses higher oxide layer thickness and oxygen content, but the flowability is increased, suggesting better spreadability and packing of the powder bed. Fig. 9(a, b) illustrates a comparison of Cr2p spectra at 0 nm and 10 nm, where the contribution from the oxide cation $Cr2p^{3+}$ becomes more prominent with conditioning and curing of the powder at 10 nm, thus indicating higher thickness and fraction of Cr in the oxidized state. In Fig. 9(c), it is also apparent that there is a satellite peak close to 719 eV, that is characteristic of Fe-rich hydroxide presence and has $\Delta E = 8.2$ eV from the main $Fe2p^{3+}_{3/2}$ peak.

Fig. 10 shows the cation concentration in the surface oxide of the powders as a function of etch depth. Notice that the increase in Mn^{ox} with sputtering does not mean that the Mn^{ox} is increasing. During sputtering, other cations are removed much faster. Trace oxidized elements, such as Si and Nb, are removed much faster and only exist in oxidized trace amounts at the top suface. Meanwhile, Fe and Cr are removed and the metallic state of the elements is reached. In contrast, Mn remains in an oxidized state at greater depths, but its total concentration decreases with continued etching.

Initial curing of the powder causes an increase in oxygen content and the oxide layer thickness rises by approximately ~ 2 nm, also shown in Fig. 9 (c) by the absence of metallic peak in the virgin and C4 samples, but it is found that subsequent curing cycles have a lower impact on the surface chemistry and oxide layer thickness of the powder. Curing of the powder at 200 °C in air causes the Fe-based oxide layer to grow due to the reactivity of iron with oxygen at elevated temperatures.

Fig. 11 exhibits the O1s spectra of the powders for the as-received surface and after slight etching. The shoulder close to 531.5 eV, indicative of the hydroxide (OH^-) presence, is quite prominent at the as-received surface (Fig. 11 (c, e, g)) but becomes weaker after the first etching cycle. Thus, hydroxides are also present on the surface of the samples. The weaker shoulders appearing after light etching are likely a result of Si-based oxide contributions that are also located at ~ 532 eV (Fig. 11 (d, f, h)).

Similarly, the flowability of the powder increases with oxidation. The unconditioned powder possesses high avalanche energy, a metric of the energy released by an avalanche, that significantly drops with an increase in surface oxidation. The high avalanche energy in the unconditioned powder shows that the powder concentrates in large piles at the top of the bulk powder volume before collapsing at once. During BJT printing, such high cohesion would result in poor spreadability, as the powder would resist yielding to the shear forces applied by the recoater blade or compaction roller, leading to a porous and uneven powder bed. The decrease in avalanche energy with conditioning and curing shows that the surface oxidation causes the powder flow in smaller increments. The resistance of the powder to flow (break energy) improves as well, however the first 20 rpm in the virgin powder shows that there is still some friction between the particles. Packing also improves significantly with the conditioning of the powder.

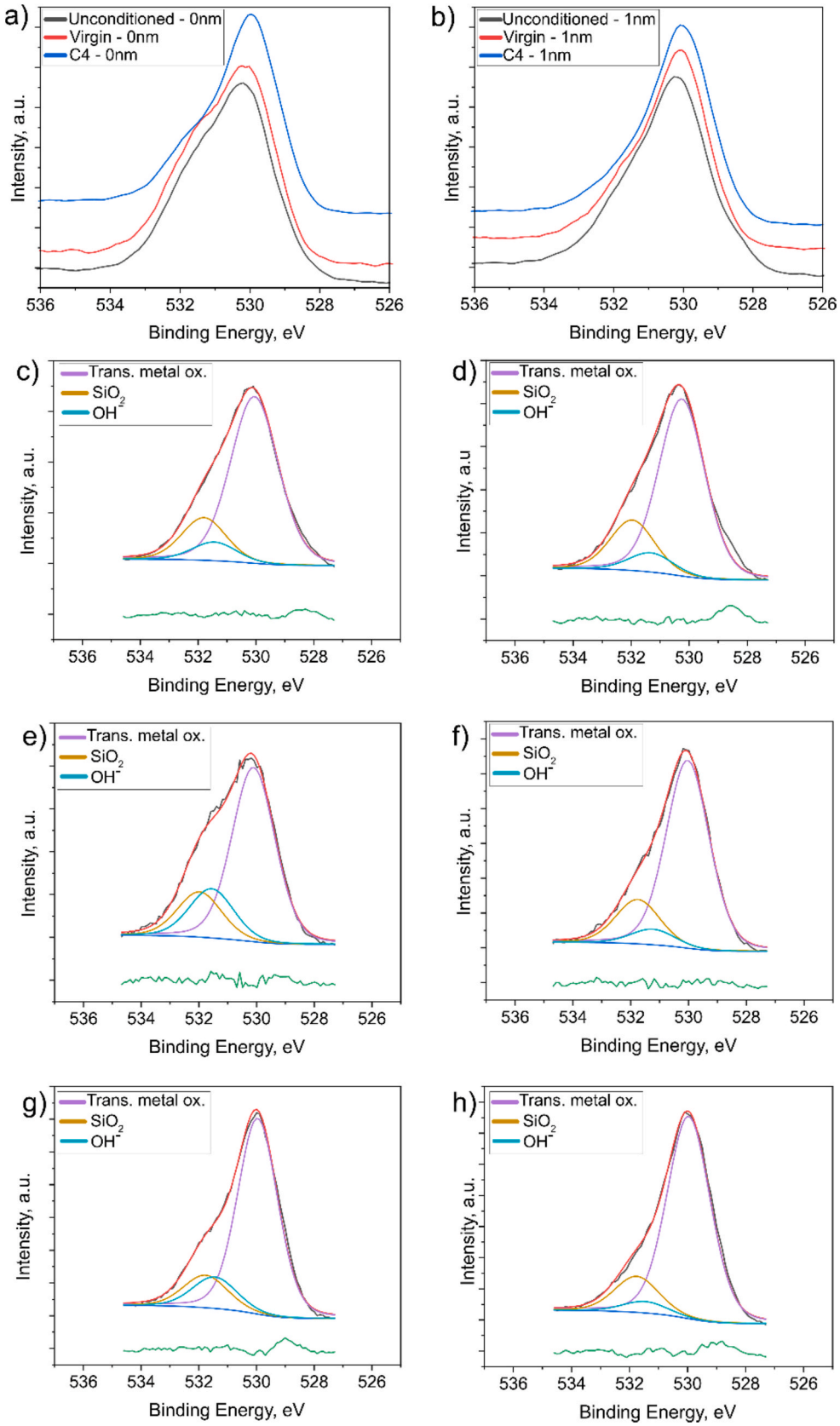

Fig. 11. Comparison of O1s spectra between the as-received (a) surfaces of the powders and after etching at 1 nm (b). Peak fitting of O1s spectra on the at the as-received surface of the c) unconditioned, e) virgin, g) C4 sample. Peak fitting of O1s spectra at 1 nm etch depth of the d) unconditioned, f) virgin, h) C4 sample.

Internal friction in the powder bulk also notably decreases (avalanche angle). A lower avalanche angle indicates that the powder requires a shallower incline to flow, which directly translates to smoother, more continuous powder spreading across the build area. Surface oxidation decreases the reactiveness of the powder surface, therefore lowering the Van der Waals forces and successfully limiting the cohesiveness of the powder due to the passivating oxide layer. The curing of the powder had a less notable positive effect on flowability and packing. The gradual coarsening of the powders (Table 3) with reuse through loss of fine particles acted in synergistic combination with the passivation of the powder to the increase in flowability. These findings strongly suggest that the surface oxidation occurring during the curing process plays a crucial role in modifying the powder's surface properties, leading to enhanced flowability. Altered powder flowability due to curing can result in inconsistent printing results, decreasing the BJT process stability, as flowability increases with the decrease of cohesion, but the mass transport phenomena also decrease with an increased oxide layer on the surface of the particles [20,32].

4.2. Connection of powder properties to part quality

The particle size distribution measurements indicated slight coarsening of the powder after 20 build jobs, potentially due to the loss of fine particles during repeated printing and sieving cycles. However, this slight change in particle size distribution alone cannot account for the substantial reduction in green density observed when printing with powder C1 after curing and sieving.

Humidity can have a substantial influence on powder rheology. The humidity increased slightly from 44 ppm to 54 ppm after 20 build jobs including four curing cycles. During curing, the powder is both dried and oxidized. A decrease in humidity after curing from virgin powder to C1 was not evident, as comparable values were obtained. Hence, the reduction in green density during printing is unlikely caused by a drying effect during the curing process. In general, the small powder sampling and environmental influences can explain minor differences in the humidity values.

The pronounced increase in bulk oxygen content and oxide layer thickness from the virgin powder to the C1 powder correlated with the most significant decrease in the green density of the printed samples. Since all printing parameters were kept constant, the decrease in green densities is attributed to changes in the powder packing behavior within the powder bed during printing. From C1 to C3, the bulk oxygen content and oxide layer thickness increased only slightly, which was accompanied by a minor decrease in the green densities. The variations in the green densities increased considerably for printing with C3 powder, indicating reduced process stability compared to printing with virgin powder.

To ensure a robust and reproducible printing process, the relevant powder characteristics must remain consistent throughout repeated powder reuse cycles. Curing in air has a detrimental impact on the green densities of printed parts, which is caused by a change in 17-4 PH powder characteristics due to powder oxidation during curing. This decrease in green density due to powder reuse after curing in air affects the sintering shrinkage and leads to lower sintered part densities [33]. One potential strategy to maintain consistent powder characteristics for powder reuse is to perform curing in an inert atmosphere, such as argon or nitrogen [33]. Curing under vacuum can also limit powder oxidation.

5. Conclusions

A thorough investigation on the influence of powder conditioning and curing in ambient air on powder surface chemistry and flow behavior was conducted for 17-4 PH stainless steel powder used for BJT. Unconditioned powder before any oxidation procedure was received alongside virgin powder (after the oxidation procedure aiming to improve flowability) and cured powders after printing. The unconditioned powder had a low oxygen content of ~ 730 ppm and an oxide layer thickness of ~ 4.3 nm but poor flowability. After conditioning, an uptake in oxygen content was observed, with the virgin powder possessing an oxygen content of ~ 1300 ppm. The XPS results followed the same trend, with oxide layer thickness rising to ~ 7.1 nm. The virgin powder was introduced for printing and collected after curing at 200 °C for 4 h in ambient air. The powder was sieved, reused and subjected to curing for a total of 4 cycles. The first curing process resulted in a slight growth of the bulk oxygen content at ~ 1500 ppm as well as oxide growth on the powder surface with an oxide layer thickness of ~ 9.5 nm. Throughout the curing cycles, the oxide layer thickness varied slightly, from 9.5 nm to 10 nm, and very slow progressive growth was detected. These results were in agreement with the bulk oxygen measurements, where the oxygen content was found to be mostly stable at ~ 1500 ppm for all samples collected after curing (C1-4). Conditioning of the powder had a positive impact on flowability, with all flowability and packing metrics experiencing a significant decrease after conditioning. Ultimately, the four curing cycles increased powder flowability and packing compared to the virgin powder but resulted in lower printed part quality (lower green density) and higher printing process instability.

CRediT authorship contribution statement

Sofia Kazi: Writing – original draft, Visualization, Validation, Methodology, Investigation, Formal analysis, Data curation, Conceptualization. **Kai Zissel:** Writing – review & editing, Methodology, Investigation, Formal analysis, Data curation, Conceptualization. **Eduard Hryha:** Writing – review & editing, Supervision, Resources, Project administration, Funding acquisition, Data curation, Conceptualization.

Declaration of competing interest

The authors declare the following financial interests/personal relationships which may be considered as potential competing interests: Sofia Kazi reports financial support was provided by Swedish Governmental Agency of Innovation Systems (Vinnova). Kai Zissel reports financial support was provided by Federal Ministry of Research and Education (BMBF, Germany). If there are other authors, they declare that they have no known competing financial interests or personal relationships that could have appeared to influence the work reported in this paper.

Acknowledgments

This work was conducted in the framework of the Centre for Additive Manufacturing – Metal (CAM^2), supported by the Swedish Governmental Agency of Innovation Systems (Vinnova). Linde GmbH acknowledges the funding by the Federal Ministry of Research and Education (BMBF, Germany), for the project SINEWAVE (FKZ 03HY123A) within the Hydrogen Flagship Project H2Giga.

Appendix A. Supplementary data

Supplementary data to this article can be found online at https://doi.org/10.1016/j.apsusc.2026.168270.

Data availability

Data will be made available on request.

References

[1] S. Mirzababaei, S. Pasebani, A review on binder jet additive manufacturing of 316L stainless steel, J. Manuf. Mater. Process. 3 (3) (2019), https://doi.org/10.3390/jmmp3030082.

[2] A. Cabo Rios, E. Hryha, E. Olevsky, P. Harlin, Sintering anisotropy of binder jetted 316L stainless steel: part I–sintering anisotropy, Powder Metall. 65 (4) (2022) 273–282, https://doi.org/10.1080/00325899.2021.2020485.
[3] I. Rishmawi, M. Salarian, M. Vlasea, Tailoring green and sintered density of pure iron parts using binder jetting additive manufacturing, Addit. Manuf. 24 (2018) 508–520, https://doi.org/10.1016/J.ADDMA.2018.10.015.
[4] M. Ziaee, N.B. Crane, Binder jetting: a review of process, materials, and methods, Addit. Manuf. 28 (2019) 781–801, https://doi.org/10.1016/J.ADDMA.2019.05.031.
[5] H. Miyanaji, K.M. Rahman, M. Da, C.B. Williams, Effect of fine powder particles on quality of binder jetting parts, Addit. Manuf. 36 (2020), https://doi.org/10.1016/j.addma.2020.101587.
[6] A. Shad, R. Stache, A. Rütjes, Effects of fumed silica flow aids on flowability and packing of metal powders used in Binder-Jetting additive manufacturing process, Mater. Des. 212 (2021) 110253, https://doi.org/10.1016/J.MATDES.2021.110253.
[7] Y. Bai, G. Wagner, C.B. Williams, Effect of particle size distribution on powder packing and sintering in binder jetting additive manufacturing of metals, J. Manuf. Sci. Eng. 139 (8) (2017), https://doi.org/10.1115/1.4036640.
[8] B. Barthel, F. Janas, S. Wieland, Powder condition and spreading parameter impact on green and sintered density in metal binder jetting, Powder Metall. 64 (5) (2021) 378–386, https://doi.org/10.1080/00325899.2021.1912923.
[9] K. Janzen, K.J. Kallies, L. Waalkes, P. Imgrund, C. Emmelmann, Influence of different powder conditioning strategies on metal binder jetting with Ti-6Al-4V, Materials 17 (3) (2024), https://doi.org/10.3390/ma17030750.
[10] P. Nandwana, A.M. Elliott, D. Siddel, A. Merriman, W.H. Peter, S.S. Babu, Powder bed binder jet 3D printing of Inconel 718: Densification, microstructural evolution and challenges☆, Curr. Opin. Solid State Mater. Sci. 21 (4) (2017) 207–218, https://doi.org/10.1016/j.cossms.2016.12.002.
[11] S. Mirzababaei, B.K. Paul, S. Pasebani, Metal powder recyclability in binder jet additive manufacturing, JOM, 72, 10.1007/s11837-020-04258-6.
[12] P. Bidare, R. Abdullah, A. Jiménez, K. Essa, Powder reusability in metal binder jetting, Proc. Inst. Mech. Eng., Part E: J. Process Mech. Eng. 238 (4) (2024) 1554–1560, https://doi.org/10.1177/09544089221147778.
[13] C. Schwerz, A. Raza, X. Lei, L. Nyborg, E. Hryha, H. Wirdelius, In-situ detection of redeposited spatter and its influence on the formation of internal flaws in laser powder bed fusion, Addit. Manuf. 47 (2021) 102370, https://doi.org/10.1016/J.ADDMA.2021.102370.
[14] G. Soundarapandiyan, et al., The effects of powder reuse on the mechanical response of electron beam additively manufactured Ti6Al4V parts, Addit. Manuf. 46 (2021) 102101, https://doi.org/10.1016/J.ADDMA.2021.102101.
[15] N. Emminghaus, C. Hoff, J. Hermsdorf, S. Kaierle, Residual oxygen content and powder recycling: effects on surface roughness and porosity of additively manufactured Ti-6Al-4V, Addit. Manuf. 46 (2021) 102093, https://doi.org/10.1016/J.ADDMA.2021.102093.
[16] B. Barthel, M. Mirz, F. Petzoldt, Process development of grade A11 high carbon tool steel for metal binder jetting, World PM 2022 Congress Proceedings, 2022, doi: 10.59499/WP225367264.
[17] D. Riabov, L. Cordova, E. Hryha, S. Bengtsson, Effect of powder variability on laser powder bed fusion processing and properties of 316L, Eur. J. Mater. 2 (1) (2022) 202–221, https://doi.org/10.1080/26889277.2022.2064772.
[18] D. Riabov, E. Hryha, M. Rashidi, S. Bengtsson, L. Nyborg, Effect of atomization on surface oxide composition in 316L stainless steel powders for additive manufacturing, Surf. Interface Anal. 52 (11) (2020) 694–706, https://doi.org/10.1002/sia.6846.
[19] O. Bergman, Influence of oxygen partial pressure in sintering atmosphere on properties of Cr-Mo prealloyed powder metallurgy steel, Powder Metall. 50 (3) (2007) 243–249, https://doi.org/10.1179/174329007X205073.
[20] E. Hryha, E. Dudrova, L. Nyborg, On-line control of processing atmospheres for proper sintering of oxidation-sensitive PM steels, J. Mater. Process. Technol. 212 (4) (2012) 977–987, https://doi.org/10.1016/J.JMATPROTEC.2011.12.008.
[21] K. Zissel, E. Bernardo, P. Forêt, E. Hryha, Impact of oxygen content on debinding of binder jetted 17-4 PH stainless steel: part I – debinding, Powder Metall. 68 (1) (2025) 3–15, https://doi.org/10.1177/00325899241307824/FORMAT/EPUB.
[22] K. Zissel, E. Bernardo, P. Forêt, E. Hryha, Impact of oxygen content on debinding of binder jetted 17-4 PH stainless steel: part II – sintering, Powder Metall. 68 (1) (2025) 16–28, https://doi.org/10.1177/00325899241307871/FORMAT/EPUB.
[23] "20240514_MDS_Studio2_PureSinter_17-4PH".
[24] L. Nyborg, A. Nylund, I. Olefjord, Thickness determination of oxide layers on spherically-shaped metal powders by ESCA, Surf. Interface Anal. 12 (2) (1988) 110–114, https://doi.org/10.1002/sia.740120209.
[25] C. Oikonomou, E. Hryha, L. Nyborg, Development of methodology for surface analysis of soft magnetic composite powders, in Surface and Interface Analysis, (2012), 1166–1170. doi: 10.1002/sia.3848.
[26] E. Hryha, C. Gierl, L. Nyborg, H. Danninger, E. Dudrova, Surface composition of the steel powders pre-alloyed with manganese, Appl. Surf. Sci. 256 (12) (2010) 3946–3961, https://doi.org/10.1016/J.APSUSC.2010.01.055.
[27] J. Wendel, S.K. Manchili, E. Hryha, L. Nyborg, Reduction of surface oxide layers on water-atomized iron and steel powder in hydrogen: effect of alloying elements and initial powder state, Thermochim Acta 692 (2020) 178731, https://doi.org/10.1016/J.TCA.2020.178731.
[28] C.D. Wagner, Handbook of x-ray photoelectron spectroscopy: a reference book of standard data for use in x-ray photoelectron spectroscopy. Perkin-Elmer Co., Physical Electronics Division, 1979. Accessed: Feb. 26, 2025. [Online]. Available: https://cir.nii.ac.jp/crid/1130000794672797312.bib?lang=en.
[29] M. Hellwig, et al., Stabilization of amide-based complexes of niobium and tantalum using malonates as chelating ligands: precursor chemistry and thin film deposition, Chem. Mater. 19 (25) (2007) 6077–6087, https://doi.org/10.1021/CM0630441.
[30] H. Karlsson, L. Nyborg, S. Berg, Surface chemical analysis of prealloyed water atomised steel powder, Powder Metall. 48 (1) (2005) 51–58, https://doi.org/10.1179/0032589005X37675.
[31] M.V Glazoff, N. Soelberg, On a Thermodynamic approach to material selection for service in aggressive multi-component gaseous and/or vapor environments, 2015, doi: 10.13140/RG.2.1.1390.6648.
[32] Z.A. Munir, Analytical treatment of the role of surface oxide layers in the sintering of metals, J. Mater. Sci. 14 (11) (1979) 2733–2740, https://doi.org/10.1007/BF00610647/METRICS.
[33] K. Zissel, S. Dubiez-Le Goff, E. Hryha, Binder jetting – Impact of powder reuse and curing on powder characteristics, green parts and sintering densification of 17-4 PH stainless steel, Powder Metallurgy 0 (0) (2026), https://doi.org/10.1177/00325899261479464.